

Phase diagram of silica from computer simulationIvan Saika-Voivod,¹ Francesco Sciortino,^{1,2} Tor Grande,³ and Peter H. Poole⁴¹*Dipartimento di Fisica and Istituto Nazionale per la Fisica della Materia, Università di Roma La Sapienza, Piazzale Aldo Moro 2, I-00185, Roma, Italy*²*INFN-CRS SOFT: Complex Dynamics in Structured Systems, Università di Roma La Sapienza, Piazzale Aldo Moro 2, I-00185, Roma, Italy*³*Department of Materials Technology, Norwegian University of Science and Technology, N-7491 Trondheim, Norway*⁴*Department of Physics, St. Francis Xavier University, Antigonish, Nova Scotia, Canada B2G 2W5*

(Received 8 June 2004; published 29 December 2004)

We evaluate the phase diagram of the “BKS” potential [van Beest, Kramer, and van Santen, *Phys. Rev. Lett.* **64**, 1955 (1990)], a model of silica widely used in molecular dynamics (MD) simulations. We conduct MD simulations of the liquid, and three crystals (β -quartz, coesite, and stishovite) over wide ranges of temperature and density, and evaluate the total Gibbs free energy of each phase. The phase boundaries are determined by the intersection of these free energy surfaces. Not unexpectedly for a classical pair potential, our results reveal quantitative discrepancies between the locations of the BKS and real silica phase boundaries. At the same time, we find that the topology of the real phase diagram is reproduced, confirming that the BKS model provides a satisfactory qualitative description of a silicalike material. We also compare the phase boundaries with the locations of liquid-state thermodynamic anomalies identified in previous studies of the BKS model.

DOI: 10.1103/PhysRevE.70.061507

PACS number(s): 64.70.Ja, 81.30.Dz, 64.30.+t

I. INTRODUCTION

The melts of silica, water, and a number of other substances at ambient pressure P form so-called “tetrahedral liquids,” that is, liquids with properties that are strongly influenced by the occurrence of a network of tetrahedrally arranged atoms. This class of substances includes other molecular systems of AB_2 stoichiometry (e.g., GeO_2 and BeF_2), as well as atomic systems (e.g., Si and C). Such liquids display a rich spectrum of behavior, including density maxima [1], dynamical anomalies [2], as well as the ability to form numerous crystal polymorphs [3]. Evidence also exists that liquid-liquid phase transitions occur in some of these systems [4–6]. Yet a detailed understanding of the commonalities among these materials is hampered by our incomplete knowledge of their properties under comparable conditions. For example, we have extensive knowledge of liquid water for temperatures T near and above the melting temperature T_m for $T \geq 0.85T_m$, but the behavior below this range remains a subject of debate [7]. Conversely, we have detailed knowledge of molten silica at ambient P for $T \leq T_m$, but a much less complete picture of the behavior at higher T and P [8].

Computer simulations have contributed to filling this knowledge gap by providing numerical estimates of liquid behavior outside the range of current experiments. However, a key element has been missing from the description of many of these model materials: their phase diagrams. In an experimental study of a molecular liquid, knowledge of the phase diagram—that is, the coexistence boundaries demarcating the stability fields of the liquid, gas, and various crystal phases—provides a vital reference that elucidates the observed thermodynamic, dynamic, and structural properties of the liquid phase. Simulations of molecular liquids are commonly based on semi-empirical classical interaction potentials that cannot be expected to precisely reproduce the experimentally known phase diagrams of the real material. It is

perhaps for this reason that comprehensive phase diagrams have not yet been developed for the simulation models used widely to study the complexities of important molecular liquids, such as water and silica. However, as a consequence, it has not been possible to self-consistently relate the behavior found in simulations to the relevant phase boundaries of the model system, as would normally occur in an experimental study.

With these motivations, we here focus on the van Beest, Kramer, and van Santen (BKS) model of silica [9]. The BKS model has played an important role over the last decade in numerous studies of silica and related materials. For example, the BKS model has been used in studies of pressure-induced amorphization of quartz [10], the α - to β -quartz phase transition [11,12], the fragile-to-strong dynamical crossover in liquid silica [13–15], the possibility of liquid-liquid phase separation in silica [5], and in the study of the generic topological and entropic properties of random tetrahedral networks [16]. Despite this interest in the BKS model, only fragments of specific crystal-crystal phase boundaries have been located, such as the α - to β -quartz transition. To our knowledge no data currently exist for the melting lines, though the liquid-gas coexistence curve has been located for a model similar to that of BKS [17]. In this paper we report the phase diagram of the BKS model, finding the stability fields in the P - T plane for the liquid phase, and three of the prominent crystal phases of real silica, stishovite, coesite, and β -quartz.

II. METHODS

We use the BKS potential, modified at short range to prevent unphysical “fusion” events, and at long range to reduce

the system size dependence of measured properties and to facilitate determination of minimum energy structures (“inherent structures”). Reference [15] provides a detailed specification of the modified potential, a summary of which is provided in the Appendix of the present work. Results obtained with our modified potential differ little from those found using the original BKS potential in terms of averaged structural and dynamical behavior. As described in Ref. [15], the values of thermodynamic properties are slightly shifted compared to the original BKS potential, but the qualitative behavior is unaffected. The Coulombic contribution to the energy is evaluated via the Ewald method, where the reciprocal space summation is carried out to a radius of nine times the smallest reciprocal cell width [18]. In all cases, the time step used in our molecular dynamics (MD) simulations is 1 fs.

We restrict our attention to the liquid phase, and the crystal phases stishovite, coesite, and β -quartz. A number of other crystal phases of silica are known. However, the stability fields of these three crystals dominate the phase diagram of silica on the widest scale of P and T , and are therefore natural first choices for examination [3]. These three crystals are also representative of the main types of local coordination structures found in silica crystals. The structure of β -quartz is an open network of corner-shared SiO_4 tetrahedra; coesite is a denser network of corner-shared SiO_4 tetrahedra; and stishovite is a network of corner- and edge-shared SiO_6 octahedra. Previous work has shown that the BKS model is appropriate for studying both low and high density crystal structures [19]. To determine the phase diagram, our approach is to evaluate numerically the Gibbs free energy G of each of the phases as a function of P and T , and then seek the lines of intersection of these surface functions.

A. Liquid free energy

For the liquid phase, we use much of the equation of state data reported in Ref. [15], plus some new simulation data generated using the same methodology. These simulations modeled a system of a fixed number of 444 molecular units (1332 ions) in the liquid phase along nine isochores from volumes $V=4.6296$ to $8.6804 \text{ cm}^3 \text{ mol}^{-1}$, and ranging in T from nearly 7000 to less than 2500 K (Fig. 1). Each of these liquid state points was equilibrated at constant V , and using velocity rescaling to attain a desired T . Average values of P and T were evaluated from subsequent constant- NVE runs having a duration of ten times the time required for silicon atoms to diffuse an average of 0.2 nm. The results provide the total energy $E(T)$ (potential plus kinetic) and $P(T)$ along the specified isochores. Reference [15] also describes the details of a calculation of the entropy of the liquid phase, $S_R = 75.986 \pm 0.176 \text{ J mol}^{-1} \text{ K}^{-1}$, at a reference state located at $T_R=4000 \text{ K}$ and $V_R=8.6804 \text{ cm}^3 \text{ mol}^{-1}$.

The value of E at an arbitrary point (V_o, T_o) on the surface $E(V, T)$ is evaluated as follows. Along each of the nine isochores simulated, a third order polynomial in T is fitted to the E data. The value of E at the desired $T=T_o$ is calculated from the polynomial found for each V . This creates a set of points approximating the curve $E(V)$ at $T=T_o$. A cubic spline pass-

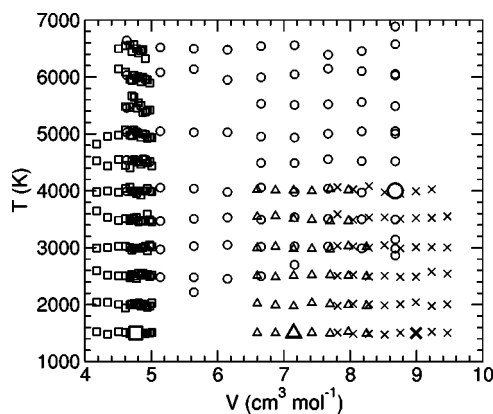


FIG. 1. Location of points in the V - T plane at which we conduct simulations of the liquid (circles), stishovite (squares), coesite (triangles), and β -quartz (crosses). The large symbols locate reference states (V_R, T_R) at which the entropy of each phase is evaluated directly.

ing through these points is then found, creating a continuous function representing $E(V)$ at $T=T_o$. The value of E at the point (V_o, T_o) is evaluated from this function. The value of P at an arbitrary point (V_o, T_o) is calculated in exactly the same way as for E , except that a fourth order polynomial in T is fitted to the P data along each of the nine simulated isochores. Examples of the simulated and fitted values of E and P are shown in Fig. 2.

The value of S at an arbitrary point (V_o, T_o) is evaluated by thermodynamic integration, using the $E(V, T)$ and $P(V, T)$ surfaces constructed as described above. The integration is given by

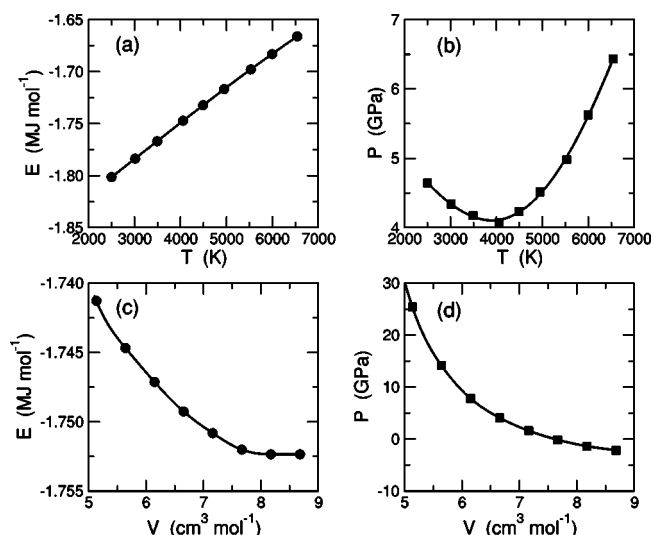


FIG. 2. Examples of fitted and interpolated data for the liquid phase: (a) values of E along the $V=6.655 \text{ cm}^3 \text{ mol}^{-1}$ isochore, fitted with a cubic polynomial (line); (b) values of P for $V=6.655 \text{ cm}^3 \text{ mol}^{-1}$, fitted with a quartic polynomial (line); (c) interpolated values of E along the $T=4000 \text{ K}$ isotherm, fitted with a cubic spline (line); (d) interpolated values of P for $T=4000 \text{ K}$, fitted with a cubic spline (line).

$$S(V_o, T_o) = S_R + \int_{T_R}^{T_o} \frac{1}{T} \left(\frac{\partial E}{\partial T} \right)_{V_R} dT + \frac{1}{T_o} \int_{V_R}^{V_o} P(V, T_o) dV. \quad (1)$$

The definite integral over T is evaluated analytically using the polynomial representation of E as a function of T , on the reference isochore. The definite integral over V is evaluated numerically via Simpson's rule, using data from the cubic spline representation of P as a function of V , constructed along the desired isotherm.

We combine these numerical estimates to determine the Gibbs free energy G at arbitrary state points using $G(V, T) = E(V, T) + VP(V, T) - TS(V, T)$. To find G at an arbitrary (P, T) point, we find the value of V from $P(V, T)$ such that P has the desired value. In this way we can construct arbitrary isotherms or isobars cutting through the $G(P, T)$ surface.

B. Crystal free energy

We conduct simulations of three crystal phases: stishovite, β -quartz, and coesite. Our simulations employ 1200 ions for stishovite, 1536 ions for coesite, and 1350 ions for β -quartz. We carry out simulations over a range of V and T appropriate for each phase, as shown in Fig. 1.

We employ the following procedure to obtain equilibrium averages for $E(T)$ and $P(T)$ along the specified isochores. The rationale underlying this procedure is to allow us to obtain thermodynamic properties along a set of specified isochores, so that we may construct the $G(P, T)$ surface for each phase in the same way as described above for the liquid phase. However, obtaining isochoric data for crystals requires care, as unit cell parameters may change with T , even though the overall density remains fixed. In particular, we must ensure that anisotropic stresses do not arise in the simulation cell. The procedure, for each crystal, is as follows.

First, we create an initial configuration of stishovite, β -quartz [20], and coesite [21]. Then for a number of specified V , we optimize the $T=0$ atomic coordinates and unit cell parameters to minimize the energy and to remove anisotropic stresses. This optimization is carried out at constant overall V , and consists of alternating applications of the simplex method (to optimize cell parameters) and the conjugate gradient method (to optimize atomic coordinates) [22]. This optimization cycle is repeated until the energy converges to a minimum value to within a tolerance of 10^{-10} .

Then, for each T at which we desire thermodynamic properties, we carry out the following steps.

(i) Beginning with the optimized configuration at the appropriate V , we conduct a 20 ps constant- V simulation, during which the desired T is established via velocity rescaling every 100 time steps.

(ii) The configuration produced in (i) is used to initiate a 20 ps constant- NVE simulation, to ensure that an equilibrium state at the desired T has been achieved.

(iii) To relax any anisotropic stress that may have arisen in bringing the system to nonzero T , we carry out a 40 ps constant- NPT simulation (during which the simulation cell geometry is unconstrained) where we set P to the average value from step (ii).

(iv) Step (iii) may have changed the overall V of the simulation cell away from the desired isochore. We restore the value of V of the simulation cell by isotropically rescaling the average cell lengths obtained in step (iii), while leaving the obtained average angles fixed. For all crystals, the rescaling is never more than 0.5% of the desired volume, and is typically 0.1%. This rescaled configuration is then used to initiate a 30 ps constant- NVE simulation, during which the average values of P and T are evaluated.

We note that for β -quartz, step (iii) is carried out for 50 ps and step (iv) for 80 ps. These longer times are used in order to resolve the subtle variation of P along isochores, since β -quartz displays a density maximum in the region of our simulations. We also note that the β -quartz phase spontaneously converts to α -quartz, but only for T and V outside the range of simulated points shown for β -quartz in Fig. 1. Our results therefore pertain only to β -quartz and are not influenced by this crystal-crystal phase transition.

The above procedure provides $E(T)$ and $P(T)$ along specified isochores. Using the same fitting and interpolation procedure as is used for the liquid, we can therefore evaluate E and P at arbitrary state points (V, T) .

Finally, we need to evaluate S for each crystal at a reference state point, in order to construct the surface $S(V, T)$ via thermodynamic integration. Our method is as follows. For each crystal phase we select a reference volume V_R (see Fig. 1), and choose the $T_R=1500$ K configuration obtained at the end of step (iv) above. Using the conjugate gradient method, we optimize the atomic positions (at fixed cell geometry) to find the minimum energy configuration. We then evaluate the Hessian matrix of this minimum energy configuration and diagonalize it to find the eigenfrequency spectrum. The classical harmonic entropy is found from this eigenfrequency spectrum. (The details of this approach are given in Ref. [15], where the method is used to find the classical harmonic entropy of inherent structures of the liquid state.)

To determine the total entropy, we need to evaluate the anharmonic contribution and add it to the harmonic entropy found above. We use the energy-optimized configuration for which we calculate the harmonic entropy as the starting configuration for 15 equally spaced simulations from $T=100$ K to $T_R=1500$ K. We simulate each state point at constant V using velocity scaling to maintain T at the desired value, with fixed cell geometry, for 150 ps (400 ps for stishovite). From these simulations we evaluate

$$E_{anh}(T) = U(T) - \frac{3}{2}R(1 - 1/N)T, \quad (2)$$

where U is the potential energy and R is the gas constant. Using a polynomial fit,

$$E_{anh} = a_0 + \sum_{n=2}^{N_{max}} a_n T^n, \quad (3)$$

we evaluate

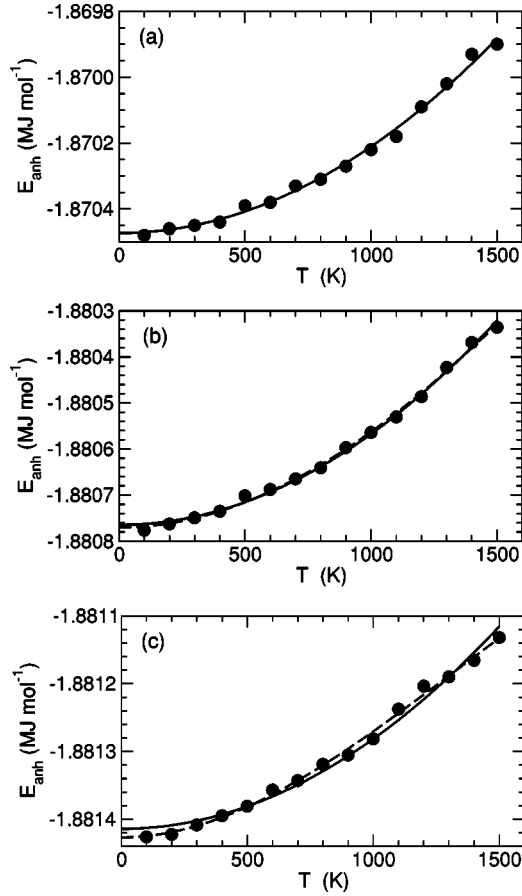


FIG. 3. $E_{anh}(T)$ for (a) β -quartz, (b) coesite, and (c) stishovite along their respective reference isochores. In (a) the solid line is the fit to the data given by Eq. (3) with $N_{max}=2$. The fit for $N_{max}=3$ is not visible as it overlaps with the $N_{max}=2$ curve on the scale of this plot. In (b) the fits for both $N_{max}=2$ (solid) and $N_{max}=3$ (dashed) are shown. In (c) the fits for $N_{max}=2$ (solid) and $N_{max}=4$ (dashed) are shown, while the curve for $N_{max}=3$ is not visible as it overlaps with the $N_{max}=4$ curve.

$$S_{anh}(T_R) = \int_0^{T_R} \frac{1}{T} \left(\frac{\partial E_{anh}(T)}{\partial T} \right)_V dT. \quad (4)$$

By using different values of $N_{max}=2$ and 3 for coesite and β -quartz, and 3 and 4 for stishovite, we obtain error estimates for $S_{anh}(T_R)$. Figure 3 shows the variation of E_{anh} with T for each of the three crystals simulated. The resulting reference entropies for each crystal phase at $T_R=1500$ K at their respective reference volumes V_R are as follows: $44.982 \text{ J mol}^{-1} \text{ K}^{-1}$ at $V_R=8.9933 \text{ cm}^3 \text{ mol}^{-1}$ for β -quartz; $43.682 \text{ J mol}^{-1} \text{ K}^{-1}$ at $V_R=7.1478 \text{ cm}^3 \text{ mol}^{-1}$ for coesite; and $39.536 \text{ J mol}^{-1} \text{ K}^{-1}$ at $V_R=4.7650 \text{ cm}^3 \text{ mol}^{-1}$ for stishovite. The uncertainty in each S value is approximately $0.01 \text{ J mol}^{-1} \text{ K}^{-1}$.

The above procedure provides $E(V, T)$, $P(V, T)$, and the reference value of S for each of the three crystal phases. The procedure to evaluate $G(P, T)$ from this information for each crystal phase is the same as is used for the liquid phase.

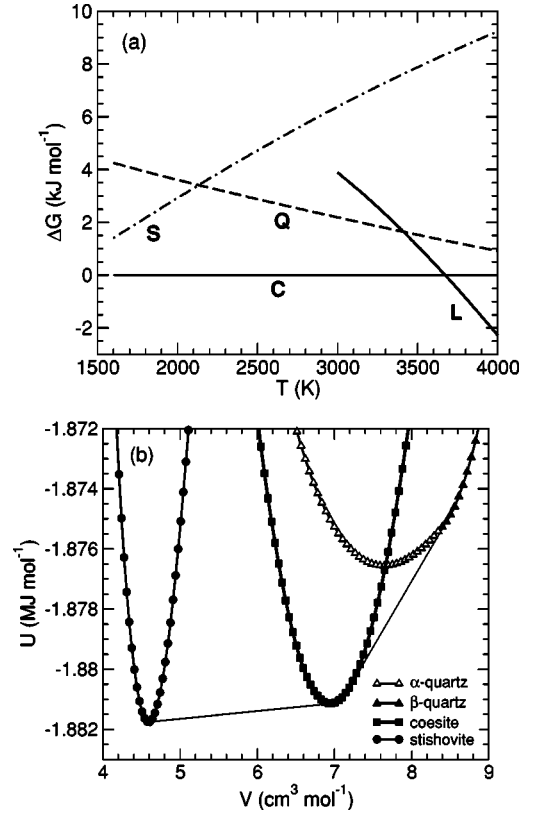


FIG. 4. (a) ΔG , the Gibbs free energy relative to that of coesite (C) for the liquid (L), β -quartz (Q), and stishovite (S) phases, at constant $P=2$ GPa. The intersections locate points on the stable and metastable coexistence lines that cross this isobar. (b) Potential energy U as function of V at $T=0$ for various crystal phases. Thin straight lines represent “common tangent constructions,” the slopes of which yield the $T=0$ coexistence pressures plotted in (b).

C. Coexistence boundaries and error estimates

For every pair of phases we determine the coexistence line as the locus of points in the plane of P and T for which G for the two phases is the same. Along each locus, we also find the value of V for each of the two coexisting phases. Figure 4(a) shows an example of the intersection of isobars of G (relative to coesite) for each phase at $P=2$ GPa.

We perform several checks on our scheme. We calculate the change in S for a single phase around a closed path in the V - T plane, which we find to be zero within an error of approximately $0.01 \text{ J mol}^{-1} \text{ K}^{-1}$. We also check that the relations $P = -(\partial A / \partial V)_T$ (where A is the Helmholtz free energy) and $P - T(\partial P / \partial T)_V = -(\partial E / \partial V)_T$ are satisfactorily met. Furthermore, along the coexistence lines, we check the Clapeyron relation $dP/dT = \Delta S / \Delta V$, where ΔS is the difference in S between the two phases and ΔV is the difference in V ; we find this to be satisfied to within 0.1 MPa K^{-1} .

We also determine the stishovite/coesite and β -quartz/coesite coexistence conditions at $T=0$ by plotting the potential energy U obtained for the optimized atomic configurations used to initiate the crystal free energy calculations described in the previous section. We plot U versus V

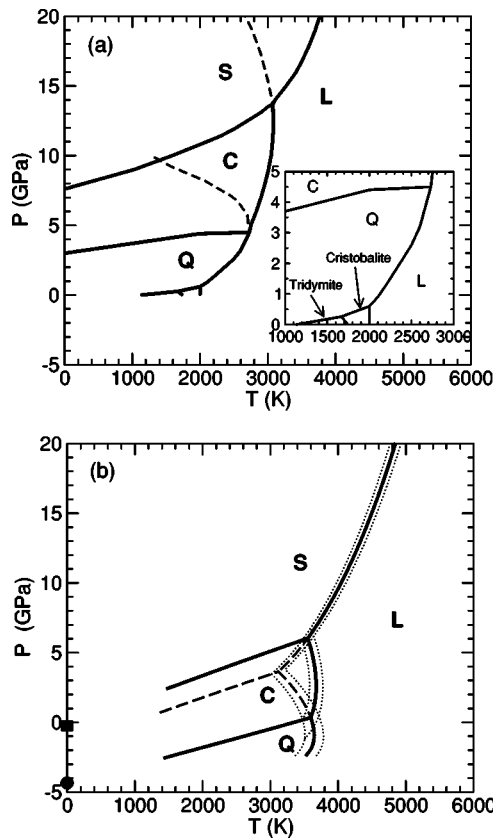


FIG. 5. (a) Experimentally determined coexistence lines of silica in the P - T plane. Stability fields for the stishovite (S), coesite (C), β -quartz (Q), and liquid (L) phases are shown. Both stable (solid) and metastable (dashed) coexistence lines are shown. The inset shows the stability fields of cristobalite and tridymite, not considered in this work. Adapted from Ref. [3]. (b) Phase diagram of BKS silica in the P - T plane. Solid lines are stable coexistence lines. Dotted lines show error estimates for the crystal-liquid coexistence lines, as described in the text. Metastable coexistence lines (dashed) are also shown that meet at the metastable S - L - Q triple point. The locations of the S - C (filled square) and C - Q (filled circle) coexistence boundaries at $T=0$, determined from Fig. 4(b), are also shown.

at $T=0$ in Fig. 4(b) and extract the coexistence pressures from the slope of “common tangent constructions” bridging coexisting phases. The $T=0$ coexistence pressures are plotted in Fig. 5(b) and serve to check that the method used to determine coexistence boundaries at finite T is consistent with the (more straightforward) $T=0$ evaluation. Note that we do not locate the β -quartz/stishovite coexistence condition at $T=0$ due to the fact that β -quartz transforms to α -quartz before $T=0$ is reached at the relevant volume for the common tangent construction.

Throughout the evaluation scheme described above, the largest single source of statistical error is the uncertainty cited in Ref. [15] for S_R , the entropy of the liquid at the reference state point. We therefore create confidence limits for our melting lines, shown in Fig. 5, by allowing the value of S_R to vary by $\pm 0.18 \text{ J mol}^{-1} \text{ K}^{-1}$.

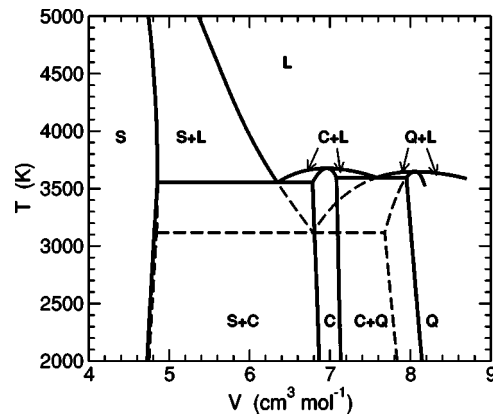


FIG. 6. Phase diagram of BKS silica in the V - T plane. The notation and symbols used have the same meaning as in Fig. 5. Note that in this projection, both one-phase stability fields as well as two-phase coexistence regions are located. The projections of the metastable coexistence lines (dashed) shown in Fig. 5 are also presented.

III. RESULTS AND DISCUSSION

Figure 5(b) plots P - T coexistence conditions, both stable and metastable, occurring among the liquid phase (L) and the crystalline phases β -quartz (Q), coesite (C), and stishovite (S). Figure 6 is the projection of the same boundaries onto the plane of V and T . This plot exposes the volume differences of coexisting phases along phase boundaries. This type of plot is rarely constructed for real materials, due to the challenge of determining the densities of coexisting phases, especially at high pressure. However, it is readily constructed from simulation data.

Comparison of the BKS and experimental phase boundaries [3] in Fig. 5 exposes the quantitative deficiencies of the model. Apparent in particular is the difference between the pressures at which corresponding features occur. For example, the S - L - C triple point occurs at 13.4 GPa in real silica, but at only 5.8 GPa in the model. Overall, the P range of the crystal stability fields is substantially lower in the model. The pressure difference between the model and reality is more of a shift than a rescaling. For example, the coesite stability field has approximately the same extent in P (about 5 GPa) at low T in both BKS and real silica. However, the S - C coexistence boundary is shifted downward in P in the model by more than 7 GPa compared to real silica. The result is that coesite, rather than quartz, is the equilibrium phase of BKS silica at ambient P for most of the temperature range. Indeed, at the very lowest T , the stishovite stability field just reaches ambient P , making stishovite the $T=0$ ground state of BKS silica at $P=0$ (filled square in Fig. 5(b)).

The correspondence of the thermal behavior is better than that of the mechanical behavior, but significant differences still occur. The T of the S - L - C and C - L - Q triple points are respectively 15% and 32% higher than their experimental values. Also, the maximum T reached by the coesite, and especially the β -quartz stability fields, are too high compared to reality. However, the curvature of the crystal-liquid coexistence boundaries are comparable to experiment.

Despite the quantitative deficiencies of the BKS model, it is noteworthy that the topology of the real silica phase diagram is reproduced in the simulations. All three studied crystals have large stability fields, which increase in extent as P increases. More subtle features, notably the melting line maxima in both the Q - L and C - L coexistence lines, are also reproduced. Also, the occurrence of a metastable S - Q - L triple point in the stability field of coesite, suggested by an extrapolation of the experimental boundaries, is observed in the model. Thus, while acknowledging its deficiencies, the BKS model is appropriate for studying the qualitative behavior of a substance with a silicalike phase diagram.

The phase information given in Figs. 5 and 6 allows previous (and future) observations of the behavior of BKS silica to be considered within the context of the phase behavior of the model itself. For example, several studies of BKS silica have identified the location of a density maximum in the liquid phase [5,13]. A thermal anomaly, a line of maxima of the isochoric specific heat C_V , has also been located in simulations of the liquid [14,15]. Both of these features have been related to the early stages of the formation of a structured tetrahedral network in the liquid state. This structural evolution also is believed to underlie a crossover from non-Arrhenian (“fragile”) to Arrhenian (“strong”) dynamics in the liquid [13–15].

We show in Fig. 7 the location of the line of density and C_V maxima in both the P - T and V - T planes. These lines approximately separate the liquid behavior into a “tetrahedral network influenced” region at low T and large V (low P), and a “normal liquid” region at high T and small V (high P). Consistent with this, the stability fields of β -quartz and coesite (both of which have four-coordinated silicon atoms) occur within the network influenced region, while the stability field of stishovite (with six-coordinated silicons) falls outside.

We also show in Fig. 7 the location of the state point at which evidence of liquid-liquid phase separation was reported in Ref. [5]. This point occurs at a density just above that of the high density edge of the one-phase stability field of coesite. This is a plausible density at which the open tetrahedral network structure of the (one-phase) supercooled liquid state begins to collapse to a higher density, perhaps via a discontinuous phase transition.

We can use the comparison of the real and simulated phase diagrams to assess the potential for finding a liquid-liquid phase transition in real silica. To be observable, the critical temperature T_c of the liquid-liquid phase transition must occur above the glass transition temperature T_g of the supercooled liquid. Choosing a common point of reference in both the BKS and real silica phase diagrams is one way to facilitate such an assessment. Here we choose the S - L - C triple point, since evidence for a liquid-liquid phase separation in BKS silica was found at about the same P as this feature. Evidence of a liquid-liquid transition in BKS silica occurs at 56% of the T of the BKS S - L - C triple point; see Fig. 7(a). The S - L - C triple point occurs in real silica at about 3100 K, 56% of which is 1730 K. This temperature is higher than $T_g=1450$ K, the glass transition temperature for real silica at ambient P . Furthermore, T_g should initially decrease in value as P increases above ambient. Although not yet

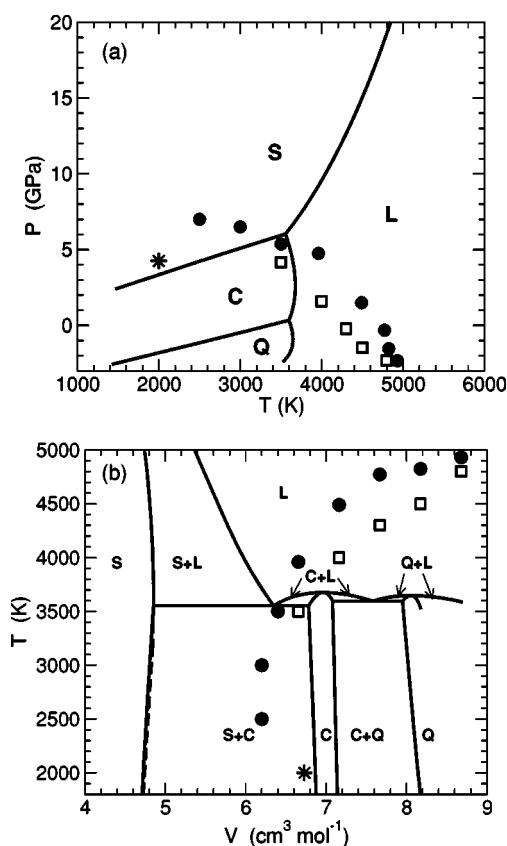


FIG. 7. BKS phase boundaries in (a) the P - T plane and (b) the V - T plane, in relation to density maxima (filled circles) and C_V maxima (squares) in the liquid phase. Also located is the state point (star) at which evidence of liquid-liquid phase separation was reported in Ref. [5].

confirmed experimentally in real silica, this is expected from the fact that the disruption of the tetrahedral network with increasing P facilitates molecular mobility, and so suppresses T_g . Ultimately the trend will reverse as packing effects begin to dominate at higher P . Based on simulation results for the diffusion coefficient of liquid BKS silica [15], the minimum value of T_g as a function of P should approximately coincide with the line of density maxima, which at low T occurs at P slightly higher than the S - L - C triple point. Hence, in BKS silica, T_g continues to decrease with P throughout the region between ambient P and that at which evidence of a liquid-liquid transition is observed. This particular assessment therefore suggests that if a liquid-liquid transition occurs in real silica, then T_c may be greater than T_g , potentially exposing the transition to direct observation.

To conclude, we note that important low pressure phases of silica, especially tridymite and cristobalite, while not addressed here, are also stable crystal phases of the BKS model. We choose not to include these phases in the present study because we want to study BKS silica over a very large range of P and T , focusing on the principal stability fields that dominate the phase diagram. That said, and in light of the results presented here, the phase behavior of these low pressure polymorphs merits attention in future work. The BKS model has been widely used to study the open network structure of silica glass. Examining its ability to reproduce

the thermodynamic relationships among all the crystal polymorphs having an open network structure would be a severe test, and would further elucidate the strengths and weaknesses of the BKS model.

ACKNOWLEDGMENTS

This research was supported by NSERC (Canada), SHARCNET, the Canada Research Chairs Program, MIUR FIRB, and PRIN.

APPENDIX

Our model of atomic interactions in silica, denoted here as Φ_{BKS} , is based on the original BKS potential, modified in two ways. First, the BKS potential energy for both the Si-O and O-O interactions diverges unphysically to negative infinity at sufficiently small distances. To prevent this, Φ_{BKS} consists of the standard BKS potential plus a short range term given by

$$4\epsilon_{\mu\nu} \left[\left(\frac{\sigma_{\mu\nu}}{r_{ij}} \right)^{30} - \left(\frac{\sigma_{\mu\nu}}{r_{ij}} \right)^6 \right] \quad (\text{A1})$$

where r_{ij} is the interatomic separation between an atom i of species μ , and an atom j of species ν . The values of the parameters $\epsilon_{\mu\nu}$ and $\sigma_{\mu\nu}$ are given in Table I, and the method by which they are chosen is described in Ref. [15].

The second modification to the standard BKS potential included in Φ_{BKS} relates to the treatment of long range interactions. As is common in implementations of the BKS potential, we calculate the long range contributions to the Coulombic potential energy using the Ewald summation technique. The reciprocal space summation is carried out here to a radius of nine reciprocal lattice cell widths. For the real space summation, instead of discontinuously cutting off the potential, as is often done, we introduce a switching function. At a fixed distance $R_s=0.77476$ nm the real space terms of the standard BKS potential are replaced by a fifth

TABLE I. Potential parameters used to define Φ_{BKS} . Also required to specify Φ_{BKS} are $\alpha=2.5$ nm⁻¹, $R_s=0.77476$ nm, $R_c=1$ nm, $q_{\text{Si}}=2.4e$, and $q_{\text{O}}=-1.2e$, where e is the magnitude of the charge of an electron.

$\mu-\nu$	Si-Si	Si-O	O-O
$A_{\mu\nu}$ (10 ⁻¹⁶ J)	0	28.845422	2.2250768
$B_{\mu\nu}$ (nm ⁻¹)	0	48.7318	27.6
$C_{\mu\nu}$ (10 ⁻²³ J nm ⁶)	0	-2.1395327	-2.8038308
$\epsilon_{\mu\nu}$ (10 ⁻²² J)	0	4.963460	1.6839685
$\sigma_{\mu\nu}$ (nm)	0	0.1313635	0.1779239
$D_{\mu\nu}$ (10 ⁻¹⁹ J/nm ⁵)	-235.3529	122.0161	-53.16278
$E_{\mu\nu}$ (10 ⁻¹⁹ J/nm ⁴)	-117.7993	61.33742	-26.25876
$F_{\mu\nu}$ (10 ⁻¹⁹ J/nm ³)	-23.83785	12.33446	-5.415203

degree polynomial that tapers smoothly to zero over the range $R_s < r_{ij} < R_c$, where $R_c=1$ nm. The values of the polynomial coefficients are given in Table I, and the method by which they are chosen is described in Ref. [15]. The Ewald parameter is assigned the value $\alpha=2.5$ nm⁻¹.

The real space contribution to Φ_{BKS} , denoted here as ϕ , is therefore a piecewise defined function of the form

$$\phi(r_{ij} \leq R_s) = \frac{q_{\mu}q_{\nu} \operatorname{erfc}(\alpha r_{ij})}{4\pi\epsilon r_{ij}} + A_{\mu\nu}e^{-B_{\mu\nu}r_{ij}} + \frac{C_{\mu\nu}}{r_{ij}^6} + 4\epsilon_{\mu\nu} \left[\left(\frac{\sigma_{\mu\nu}}{r_{ij}} \right)^{30} - \left(\frac{\sigma_{\mu\nu}}{r_{ij}} \right)^6 \right], \quad (\text{A2})$$

$$\phi(R_s < r_{ij} < R_c) = D_{\mu\nu}(r_{ij} - R_c)^5 + E_{\mu\nu}(r_{ij} - R_c)^4 + F_{\mu\nu}(r_{ij} - R_c)^3, \quad (\text{A3})$$

$$\phi(r_{ij} \geq R_c) = 0, \quad (\text{A4})$$

where $\operatorname{erfc}(x)$ is the complementary error function and ϵ is the permittivity constant.

- [1] C. Angell and H. Kanno, *Science* **193**, 1121 (1976).
 [2] F. Prielmeier, E. Lang, R. Speedy, and H. Ludemann, *Phys. Rev. Lett.* **59**, 1128 (1987).
 [3] *Silica: Physical Behavior, Geochemistry and Materials Applications*, edited by P. Heaney, C. Prewitt, and G. Gibbs, *Reviews in Mineralogy Vol. 29* (Mineralogical Society of America, Washington, D.C., 1994).
 [4] O. Mishima and H. E. Stanley, *Nature (London)* **396**, 329 (1998).
 [5] I. Saika-Voivod, F. Sciortino, and P. H. Poole, *Phys. Rev. E* **63**, 011202 (2001).
 [6] S. Sastry and C. A. Angell, *Nat. Mater.* **2**, 739 (2003).
 [7] P. G. Debenedetti, *J. Phys.: Condens. Matter* **15**, R1669 (2003).
 [8] *Structure, Dynamics and Properties of Silicate Melts*, edited by J. F. Stebbins, P. McMillan, and D. Dingwell, *Reviews in Mineralogy Vol. 32* (Mineralogical Society of America, Washington, D.C., 1995).
 [9] B. van Beest, G. Kramer, and R. van Santen, *Phys. Rev. Lett.* **64**, 1955 (1990).
 [10] J. S. Tse and D. D. Klug, *Phys. Rev. Lett.* **67**, 3559 (1991).
 [11] H. Kimizuka, H. Kaburaki, and Y. Kogure, *Phys. Rev. B* **67**, 024105 (2003).
 [12] M. Muser and K. Binder, *Phys. Chem. Miner.* **28**, 746 (2001).
 [13] J. Horbach and W. Kob, *Phys. Rev. B* **60**, 3169 (1999).
 [14] I. Saika-Voivod, P. H. Poole, and F. Sciortino, *Nature (London)* **412**, 514 (2001).
 [15] I. Saika-Voivod, F. Sciortino, and P. H. Poole, *Phys. Rev. E* **69**, 041503 (2004).
 [16] R. Vink and G. Barkema, *Phys. Rev. B* **67**, 245201 (2003).
 [17] Y. Guissani and B. Guillot, *J. Chem. Phys.* **104**, 7633 (1996).
 [18] M. Allen and D. Tildesley, *Computer Simulation of Liquids*

(Oxford University Press, Oxford, 1989).

- [19] J. S. Tse, D. D. Klug, and D. C. Allan, *Phys. Rev. B* **51**, 16392 (1995).
[20] N. Keskar and J. Chelikowsky, *Phys. Rev. B* **46**, 1 (1992).
[21] J. Smyth, J. Smith, G. Artioli, and A. Kvick, *J. Chem. Phys.*

91, 988 (1987).

- [22] W. Press, S. Teukolsky, W. Vetterling, and B. Flannery, *Numerical Recipes in FORTRAN: The Art of Scientific Computing* (Cambridge University Press, Cambridge, U.K., 1992).